INTERNATIONAL JOURNAL FOR NUMERICAL METHODS IN FLUIDS
Int. J. Numer. Meth. Fluids 2008; **57**:1669–1694
Published online 7 January 2008 in Wiley InterScience (www.interscience.wiley.com). DOI: 10.1002/fld.1700

A novel non-upwind, interconnected, multi-grid, overlapping numerical procedure for problems involving fluid flow

Mohsen M. M. Abou-Ellail*, †, Yuan Li and Timothy W. Tong

The George Washington University, 725 23rd Street, NW, Washington, DC 20052, U.S.A.

SUMMARY

A novel numerical procedure for heat, mass and momentum transfer in fluid flow is presented. The new scheme is passed on a non-upwind, interconnected, multi-grid, overlapping (NIMO) finite-difference algorithm. In 2D flows, the NIMO algorithm solves finite-difference equations for each dependent variable on four overlapping grids. The finite-difference equations are formulated using the control-volume approach, such that no interpolations are needed for computing the convective fluxes. For a particular dependent variable, four fields of values are produced. The NIMO numerical procedure is tested against the exact solution of two test problems. The first test problem is an oblique laminar 2D flow with a double step abrupt change in a passive scalar variable for infinite Peclet number. The second test problem is a rotating radial flow in an annular sector with a single step abrupt change in a passive scalar variable for infinite Peclet number. The NIMO scheme produced essentially the exact solution using different uniform and non-uniform square and rectangular grids for 45 and 30° angle of inclination. All other schemes were unable to capture the exact solution, especially for the rectangular and non-uniform grids. The NIMO scheme was also successful in predicting the exact solution for the rotating radial flow, using a uniform cylindrical-polar coordinate grid. Copyright © 2008 John Wiley & Sons, Ltd.

Received 7 August 2007; Revised 25 October 2007; Accepted 28 October 2007

KEY WORDS: multi-grid; overlapping; non-upwind; higher-order scheme; interconnected; fluid flow

INTRODUCTION

Finite-difference numerical simulations have suffered from false diffusion, which is synonymously referred to as numerical diffusion. This deficiency and other errors in computational fluid dynamics (CFD) are an inevitable outcome of the different interpolation schemes used for the convective terms. The interpolation schemes for the convective terms are classified as one-point schemes such as first-order upwind; two-point schemes such as central differencing (CD); and hybrid scheme,

*Correspondence to: Mohsen M. M. Abou-Ellail, The George Washington University, 725 23rd Street, NW, Washington, DC 20052, U.S.A.
†E-mail: abouellail@hotmail.com

which is a combination of CD and upwind differencing [1–4]. Higher-order schemes, such as three-point second-order interpolation (CUI) [5], third-order quadratic interpolation for convective kinetics (QUICK [6] and QUICK 2D [7]), four-point third-order interpolation (FPTOI) and four-point fourth-order interpolation (FPFOI) [8], offer a route to improving the accuracy of the computations. The QUICK-2D scheme is an extension of the QUICK algorithm to enhance its stability in elliptic fluid flow problems [7]. The QUICK-2D scheme utilizes a six-point quadratic interpolation surface that favors the locally upstream points [7]. All of the above schemes were unable to predict the exact profile along the y-axis the mid-plane of the first test problem of the 45° oblique flow with infinite Peclet number [8–10]. The above schemes produced uncertainties ranging from false diffusion and numerical instabilities to overshooting and undershooting [8]. Song *et al.* [9, 10] introduced a higher-order bounded discretization algorithm (weighted-average coefficient ensuring boundedness, WACEB) to overcome overshooting and undershooting encountered in their previous FPTOI and FPFOI schemes [8]. Song *et al.* [9, 10] were able to remove the overshooting and undershooting in their numerical results of the 45° oblique flow. Even the higher-order schemes, mentioned above, were also unable to predict the infinitely steep gradient of the scalar variable ϕ as it abruptly changes from zero to one in the test problem [8–10]. Raithby [11] presented a skew differencing scheme that utilizes the upstream values prevailing along the local velocity vectors at the four faces of the 2D control volume surrounding each grid node. This skew differencing scheme would capture most of the details of the oblique flow if the grid is aligned along the local velocity vectors. Raithby obtained accurate results for the problem of step change in a passive scalar using a square uniform grid of dimensions (11×11) when the flow is inclined by a 45° angle [11]. In this case one of the diagonals of the control volume (CV) surrounding each node is aligned along the uniform velocity field, while the other diagonal is perpendicular to the flow direction. Verma and Eswaran [12] used overlapping control volumes to discretize the physical solution domain. They obtained finite-difference equations that favor the upwind nodes from which the incoming flow emanates [12]. Verma and Eswaran tested their scheme using a grid of 11×11 for the step change in passive scalar in an oblique flow problem. They were unable to capture the exact solution with a square grid for the 45° flow with step changes in the passive scalar [12]. Interpolation for the convective transport is common to all of the above schemes, causing a varying degree of errors. Moreover, most of the above schemes involve upwind differencing, either explicitly or implicitly. However, the diffusive terms of the fluid flow governing equations are much easier and are more accurately modeled in most numerical schemes.

SINGLE-GRID SCHEMES

Most of the published numerical procedures use a single grid. The main governing equations can be cast in one general form, namely

$$\frac{\partial(\rho u_k \phi)}{\partial x_k} - \frac{\partial}{\partial x_k}\left(\Gamma_\phi \frac{\partial \phi}{\partial x_k}\right) = S_\phi \tag{1}$$

where u_k is the fluid velocity along coordinate direction x_k, and ϕ stands for any dependent variable such as mass fraction or dimensionless temperature. As explained by Abou-Ellail *et al.* [1], Equation (1) can be formally integrated over the control volume (CV) shown in Figure 1 to produce

DOI: 10.1002/fld

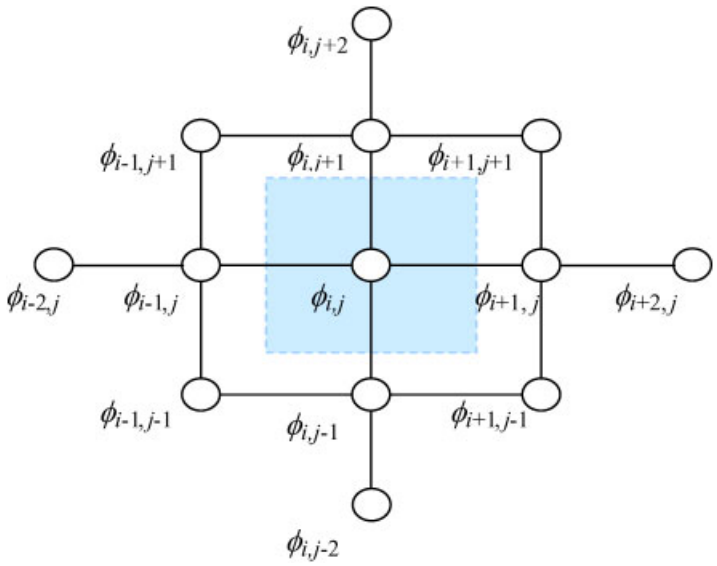

Figure 1. Control volume (CV) of single-grid schemes.

the following finite-difference equation:

$$\begin{aligned}(d_{i+1,j}+d_{i-1,j}+d_{i,j+1}+d_{i,j-1}-S_p)\phi_{i,j}\\ =d_{i+1,j}\phi_{i+1,j}+d_{i-1,j}\phi_{i-1,j}+d_{i,j+1}\phi_{i,j+1}+d_{i,j-1}\phi_{i,j-1}\\ +c_{i-1,j}\phi_{i-1/2,j}-c_{i+1,j}\phi_{i+1/2,j}+c_{i,j-1}\phi_{i,j-1/2}-c_{i,j+1}\phi_{i,j+1/2}+S_u\end{aligned} \tag{2}$$

where $d_{i+1,j}$ and $c_{i+1,j}$ are diffusion and convection coefficients to be computed at the center of the east face of the CV, midway between the central node (i) and east node $(i+1)$. They are given as

$$d_{i+1,j}=(A\Gamma_\phi/\delta x)_{\text{at } i+1/2,j} \tag{3}$$

$$c_{i+1,j}=(\rho u A)_{\text{at } i+1/2,j} \tag{4}$$

where ρ is density, u is the velocity along the x-axis, A is the east face surface area, δx is the distance between nodes i and $i+1$; Γ_ϕ is the diffusion coefficient of ϕ, and S_u and S_p are the coefficients of the integrated source term conveniently expressed as a linear expression. Equations similar to (3) and (4) apply to the west $(i-1, j)$, south $(i, j-1)$ and north $(i, j+1)$ nodes. Unlike the convective terms, the diffusion terms require no interpolation for intermediate values of ϕ. Convective terms, involving CV face values such as $\phi_{i+1/2,j}$, require interpolation between the neighboring grid nodes. The single-grid finite-difference equation can be expressed, for a central nodal point P and neighboring east–west–north–south nodes (E, W, N, S), as

$$(a_{\mathrm{E}}+a_{\mathrm{W}}+a_{\mathrm{N}}+a_{\mathrm{S}}-S_p)\phi_p=a_{\mathrm{E}}\phi_{\mathrm{E}}+a_{\mathrm{W}}\phi_{\mathrm{W}}+a_{\mathrm{S}}\phi_{\mathrm{S}}+a_{\mathrm{N}}\phi_{\mathrm{N}}+S_u \tag{5}$$

DOI: 10.1002/fld

The hybrid scheme defines the above finite-difference coefficients as follows:

$$a_{\mathrm{E}} = \max[d_{i+1,j}, |\tfrac{1}{2}c_{i+1,j}|] - \tfrac{1}{2}c_{i+1,j} \tag{6}$$

$$a_{\mathrm{W}} = \max[d_{i-1,j}, |\tfrac{1}{2}c_{i-1,j}|] + \tfrac{1}{2}c_{i-1,j} \tag{7}$$

In the above equations, max $[\cdots, \cdots]$ represents the maximum value of the two values inside the bracket. Coefficients a_{N} and a_{S} have similar expressions in the hybrid scheme. The pure upwind differencing scheme has slightly different expressions for the finite-difference coefficients.

NEW NUMERICAL SIMULATION STRATEGY

As mentioned above, most of the existing schemes, whether upwind or higher order, have a certain degree of false diffusion and/or over- and undershooting. All the above schemes cannot produce an exact numerical solution to the first test problem of a 45° oblique flow with step changes in a passive scalar for square grids [8–10] and particularly for rectangular and non-uniform grids [11]. The present simulation strategy is based on removing all the ambiguity of interpolating for the CV face values of the scalar variable ϕ. This is done simply by superimposing four grids on the 2D solution domain. These grids are arranged in such a way that each grid uses the remaining grids to obtain directly, without any interpolations, the CV face values of the scalar variable used in computing the convective terms. The present new scheme essentially replaces the interpolation process by finite-difference equations for the CV face values of ϕ. Therefore, the non-upwind, interconnected, multi-grid, overlapping (NIMO) scheme eliminates most of the interpolation-based false diffusion that creeps into the numerical results. In addition to handling the scalar variables, the NIMO system can store the velocity components, pressure and its correction on same space locations. In this case, the velocity components on one grid will still be located between the pressures, and their corrections on the neighboring grids as preferred by the SIMPLE algorithm explained by Abou-Ellail *et al.* [1] and Patankar [2]. The NIMO interconnected grids share some features with the well-known staggered-grid method [1, 2]. Both methods have displaced grids, relative to a defined main grid. However, the NIMO scheme uses four overlapping grids for each dependent variable, while the staggered-grid method requires only one grid per dependent variable, as explained by Abou-Ellail *et al.* [1] and Patankar [2]. While the NIMO scheme needs no interpolations for all dependent variables, the staggered-grid method removes the need for interpolations only for the velocity components but not for the scalar variables [1, 2].

NOVEL INTERCONNECTED MULTI-GRID NUMERICAL PROCEDURE

The new NIMO system is shown in Figure 2. The main grid defines the nodes where $\phi_{i,j}$ is located in space. Three other grids are shifted in space where $\phi^{x}_{i,j}$, $\phi^{y}_{i,j}$ and $\phi^{xy}_{i,j}$ are located midway between the main-grid nodes, as shown in Figure 2. The superscripts x and y indicate shifting of grids midway with respect to the main-grid nodes. Moreover, the superscript xy indicates that the grid is shifted diagonally such that the shifted nodes occupy the center node between the

DOI: 10.1002/fld

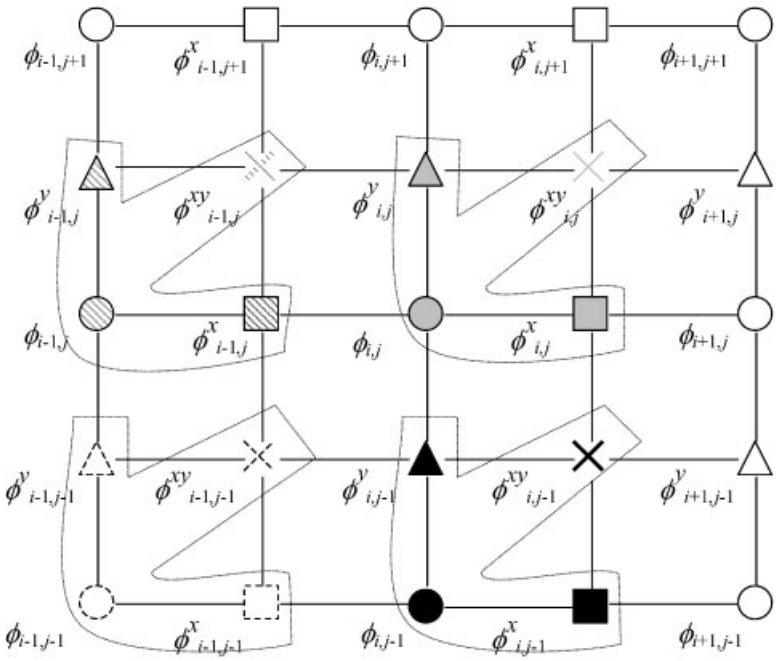

Figure 2. NIMO coordinate system, defining arrow-head clusters, of nodes with same indices, but differ in their spatial locations, in the main, x-, y- and xy-grids.

neighboring four nodes of the main grid. The four-node arrow-head clusters shown in Figure 2 are used to indicate the common indices (e.g. i, j) affiliated with ϕ, ϕ^x, ϕ^y and ϕ^{xy}. The spatial locations of ϕ, ϕ^x, ϕ^y and ϕ^{xy} affiliated with cluster (i, j), in the solution domain, are (x_i, y_j), $(x_i + \Delta x_i/2, y_j)$, $(x_i, y_j + \Delta y_i/2)$ and $(x_i + \Delta x_i/2, y_j + \Delta y_i/2)$, respectively. This cluster technique simplifies greatly the finite-difference equations of NIMO. It also simplifies the computer coding of the system of equations of the NIMO scheme. The NIMO control volumes CV, CV^x, CV^y and CV^{xy} are shown in Figure 3. The main grid typical control volume CV is formed by the four planes bisecting the distances between the neighboring nodes and the central node (i, j). Control volumes CV^x, CV^y and CV^{xy} enclose nodal variables $\phi^x_{i,j}$, $\phi^y_{i,j}$ and $\phi^{xy}_{i,j}$, respectively. Along the x- or y-coordinate, the faces of these CVs pass by the nearest neighboring nodes belonging to any of the four grids, as shown in Figure 3. The acting nodal and face values used for convective fluxes of the scalar variable ϕ pertaining to each control volume surrounding each node are shown in Figure 3. It should be mentioned here that the control-volume approach adopted here is similar to the finite-volume method [2]. However, in the finite-volume method, the solution domain is discretized into node-centered finite volumes [2]. With this arrangement, the computations of the convective fluxes pertaining to each control volume can be computed without the need for interpolation, even when using non-uniform grids. Firstly, the main control volume CV is considered. Equation (1) is formally integrated over the main control volume surrounding a typical node (i, j) where volume integrals are replaced by their surface integral counterparts performed over the four faces of the CV shown in Figure 3. The resulting finite-difference equation

DOI: 10.1002/fld

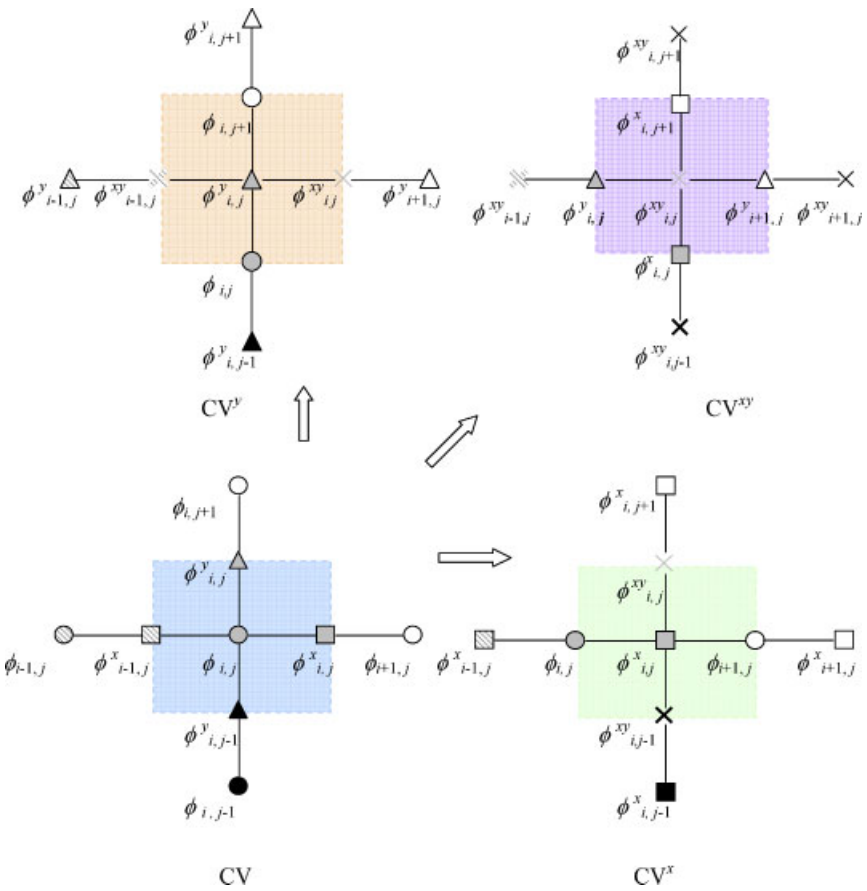

Figure 3. NIMO control volumes (CV, CV^x, CV^y and CV^{xy}) surrounding the nodes of the main, x-, y- and xy-grids.

of the main grid can be expressed as follows:

$$\begin{aligned}(d_{i+1,j}+d_{i-1,j}+d_{i,j+1}+d_{i,j-1}-S_{pi,j})\phi_{i,j}\\ =d_{i+1,j}\phi_{i+1,j}+d_{i-1,j}\phi_{i-1,j}+d_{i,j+1}\phi_{i,j+1}+d_{i,j-1}\phi_{i,j-1}\\ +c_{i-1,j}\phi^x_{i-1,j}-c_{i+1,j}\phi^x_{i,j}+c_{i,j-1}\phi^y_{i,j-1}-c_{i,j+1}\phi^y_{i,j}+S_{ui,j}\end{aligned} \tag{8}$$

The finite-difference mass continuity equation of the main-grid nodes can be expressed as follows:

$$c_{i+1,j}-c_{i-1,j}+c_{i,j+1}-c_{i,j-1}=0 \tag{9}$$

Equation (9) indicates, as it should, that the sum of the incoming mass fluxes is equal to the sum of the outgoing mass fluxes. Equations similar to (8) and (9) exist for control volumes CV^x, CV^y and CV^{xy} of the other three grids. The convective and diffusive fluxes (e.g. $d_{i+1,j}$ and $c_{i+1,j}$) are still given by Equations (3) and (4).

DOI: 10.1002/fld

Equation (8), together with similar equations for CV, CV^x, CV^y and CV^{xy}, represents a closed set of finite-difference equations for ϕ, ϕ^x, ϕ^y and ϕ^{xy}, respectively. Although they represent the same scalar variable (ϕ), they differ in their physical locations in space. However, the solution of these interconnected non-linear equations is not easy, at least with the traditional methods, e.g. tri-diagonal matrix algorithm (TDMA). Even for a passive scalar, Equation (8) has extra terms that must be included as source terms. In this case, the source terms represent passive scalar convective fluxes from the x- and y-grids to the main grid. Therefore, Equation (9) is multiplied by $\phi_{i,j}$ and is used to modify Equation (8). This modification is maneuvered such that the incoming fluxes of ϕ are added to the left-hand side, while the outgoing fluxes of ϕ are attached to the right-hand side of Equation (8). This modification helps stabilize the solutions obtained using TDMA as part of a line-by-line alternating-direction algorithm (ADA). Since TDMA is very economical in both storage and execution time demands, it has been favored over 2D-matrix-solver algorithms. Moreover, iterating between the four grids is inevitable as the solution of each grid is strongly dependent on the solutions of the other grids. The final NIMO finite-difference equations are given as follows:

$$\begin{aligned}(d_{i+1,j}+d_{i-1,j}+d_{i,j+1}+d_{i,j-1}-S_{pi,j}+c_{i+1,j}+c_{i-1,j}+c_{i,j+1}+c_{i,j-1})\phi_{i,j}\\ =d_{i+1,j}\phi_{i+1,j}+d_{i-1,j}\phi_{i-1,j}+d_{i,j+1}\phi_{i,j+1}+d_{i,j-1}\phi_{i,j-1}\\ +(c_{i-1,j}\phi^x_{i-1,j}+\tilde{c}_{i-1,j}\phi_{i,j})+(\tilde{c}_{i+1,j}\phi_{i,j}-c_{i+1,j}\phi^x_{i,j})\\ +(c_{i,j-1}\phi^y_{i,j-1}+\tilde{c}_{i,j-1}\phi_{i,j})+(\tilde{c}_{i,j+1}\phi_{i,j}-c_{i,j+1}\phi^y_{i,j})+S_{ui,j}\end{aligned} \tag{10}$$

The terms $\hat{c}$ and $\tilde{c}$ are convective fluxes expressed in a general form to allow incoming fluxes to be transferred to the left-hand side while outgoing ones appear only in the right-hand side of Equation (10). The new convective fluxes are defined along the E–W directions as

$$\hat{c}_{i-1,j}=|\tfrac{1}{2}c_{i-1,j}|+\tfrac{1}{2}c_{i-1,j} \tag{11}$$

$$\tilde{c}_{i-1,j}=\hat{c}_{i-1,j}-c_{i-1,j} \tag{12}$$

$$\hat{c}_{i+1,j}=|\tfrac{1}{2}c_{i+1,j}|-\tfrac{1}{2}c_{i+1,j} \tag{13}$$

$$\tilde{c}_{i+1,j}=\hat{c}_{i+1,j}+c_{i+1,j} \tag{14}$$

Similarly, along the N–S direction, $\hat{c}$ and $\tilde{c}$ are defined as

$$\hat{c}_{i,j-1}=|\tfrac{1}{2}c_{i,j-1}|+\tfrac{1}{2}c_{i,j-1} \tag{15}$$

$$\tilde{c}_{i,j-1}=\hat{c}_{i,j-1}-c_{i,j-1} \tag{16}$$

$$\hat{c}_{i,j+1}=|\tfrac{1}{2}c_{i,j+1}|-\tfrac{1}{2}c_{i,j+1} \tag{17}$$

$$\tilde{c}_{i,j+1}=\hat{c}_{i,j+1}+c_{i,j+1} \tag{18}$$

It can be easily shown that the sum of the four components of $\tilde{c}$ is equal to the sum of the four components of $\hat{c}$; this is done by adding Equations (12), (14), (16) and (18), i.e.

$$\begin{aligned}\tilde{c}_{i-1,j}+\tilde{c}_{i+1,j}+\tilde{c}_{i,j-1}+\tilde{c}_{i,j+1}=\hat{c}_{i-1,j}+\hat{c}_{i+1,j}+\hat{c}_{i,j-1}+\hat{c}_{i,j+1}\\ +[c_{i+1,j}-c_{i-1,j}+c_{i,j+1}-c_{i,j-1}]\end{aligned} \tag{19}$$

DOI: 10.1002/fld

The last bracket on the right-hand side of Equation (19) is equal to zero as given by Equation (9). Further simplification can be achieved if the diffusion fluxes and the convective fluxes are paired, namely,

$$\begin{aligned}(a_{i+1,j}+a_{i-1,j}+a_{i,j+1}+a_{i,j-1}-S_{pi,j})\phi_{i,j}&\\ =d_{i+1,j}\phi_{i+1,j}+d_{i-1,j}\phi_{i-1,j}+d_{i,j+1}\phi_{i,j+1}+d_{i,j-1}\phi_{i,j-1}&\\ +(c_{i-1,j}\phi^x_{i-1,j}+\tilde{c}_{i-1,j}\phi_{i,j})+(\tilde{c}_{i+1,j}\phi_{i,j}-c_{i+1,j}\phi^x_{i,j})&\\ +(c_{i,j-1}\phi^y_{i,j-1}+\tilde{c}_{i,j-1}\phi_{i,j})+(\tilde{c}_{i,j+1}\phi_{i,j}-c_{i,j+1}\phi^y_{i,j})+S_{ui,j}&\end{aligned} \tag{20}$$

It should be mentioned that Equation (20) is still equivalent to Equation (10) or Equation (8). The coefficient a on the left-hand side of Equation (20) is similar to the upwind differing coefficient, inasmuch as they both represent the net transport by convection and diffusion. However, the

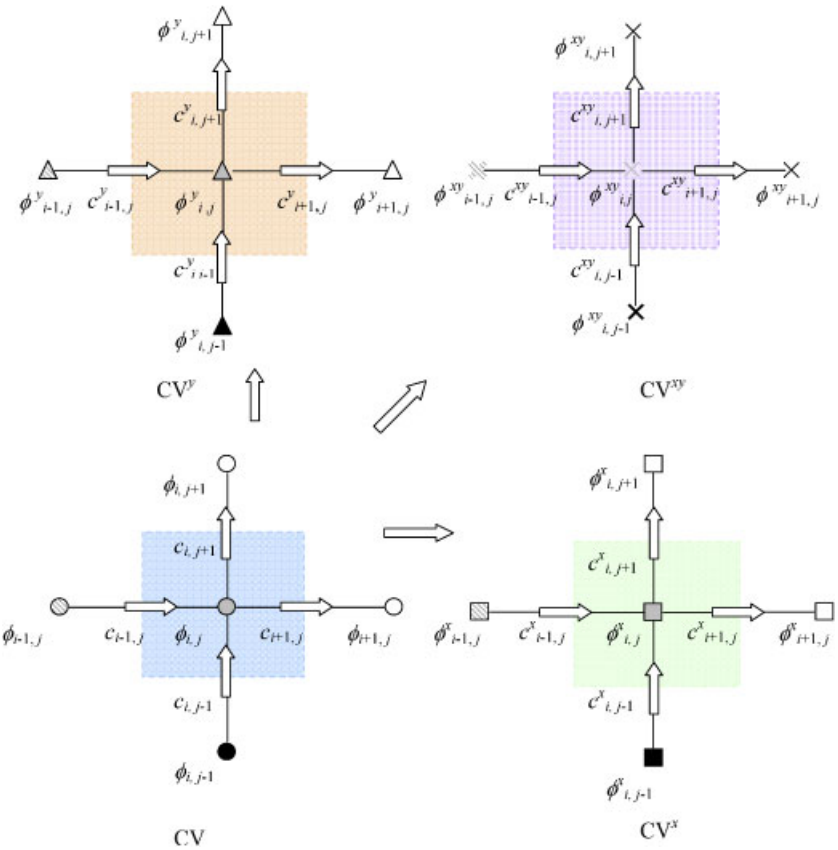

Figure 4. NIMO convective fluxes crossing the faces of CV, CV^x, CV^y and CV^{xy} control volumes of the main, x-, y- and xy-grids.

DOI: 10.1002/fld

right-hand side has a completely different structure as it accepts the outgoing fluxes. These outgoing fluxes are reduced to zero in the pure upwind scheme. Equation (20) is found to have better conversion characteristics than the final NIMO equation (Equation (10)). The above coefficients are defined as

$$a_{i+1,j} = d_{i+1,j} + \hat{c}_{i+1,j} \tag{21}$$

$$a_{i-1,j} = d_{i-1,j} + \hat{c}_{i-1,j} \tag{22}$$

$$a_{i,j+1} = d_{i,j+1} + \hat{c}_{i,j+1} \tag{23}$$

$$a_{i,j-1} = d_{i,j-1} + \hat{c}_{i,j-1} \tag{24}$$

Similarly, the NIMO finite-difference equations for control volumes CV^x, CV^y and CV^{xy} can be expressed as

$$\begin{aligned}
&(a^x_{i+1,j} + a^x_{i-1,j} + a^x_{i,j+1} + a^x_{i,j-1} - S^x_{pi,j})\phi^x_{i,j} \\
&\quad = d^x_{i+1,j}\phi^x_{i+1,j} + d^x_{i-1,j}\phi^x_{i-1,j} + d^x_{i,j+1}\phi^x_{i,j+1} + d^x_{i,j-1}\phi^x_{i,j-1} \\
&\qquad + (c^x_{i-1,j}\phi_{i,j} + \tilde{c}^x_{i-1,j}\phi^x_{i,j}) + (\tilde{c}^x_{i+1,j}\phi^x_{i,j} - c^x_{i+1,j}\phi_{i+1,j}) \\
&\qquad + (c^x_{i,j-1}\phi^{xy}_{i,j-1} + \tilde{c}^x_{i,j-1}\phi^x_{i,j}) + (\tilde{c}^x_{i,j+1}\phi^x_{i,j} - c^x_{i,j+1}\phi^{xy}_{i,j}) + S^x_{ui,j}
\end{aligned} \tag{25}$$

$$\begin{aligned}
&(a^y_{i+1,j} + a^y_{i-1,j} + a^y_{i,j+1} + a^y_{i,j-1} - S^y_{pi,j})\phi^y_{i,j} \\
&\quad = d^y_{i+1,j}\phi^y_{i+1,j} + d^y_{i-1,j}\phi^y_{i-1,j} + d^y_{i,j+1}\phi^y_{i,j+1} + d^y_{i,j-1}\phi^y_{i,j-1} \\
&\qquad + (c^y_{i-1,j}\phi^{xy}_{i-1,j} + \tilde{c}^y_{i-1,j}\phi^y_{i,j}) + (\tilde{c}^y_{i+1,j}\phi^y_{i,j} - c^y_{i+1,j}\phi^{xy}_{i,j}) \\
&\qquad + (c^y_{i,j-1}\phi_{i,j} + \tilde{c}^y_{i,j-1}\phi^y_{i,j}) + (\tilde{c}^y_{i,j+1}\phi^y_{i,j} - c^y_{i,j+1}\phi_{i,j+1}) + S^y_{ui,j}
\end{aligned} \tag{26}$$

$$\begin{aligned}
&(a^{xy}_{i+1,j} + a^{xy}_{i-1,j} + a^{xy}_{i,j+1} + a^{xy}_{i,j-1} - S^{xy}_{pi,j})\phi^{xy}_{i,j} \\
&\quad = d^{xy}_{i+1,j}\phi^{xy}_{i+1,j} + d^{xy}_{i-1,j}\phi^{xy}_{i-1,j} + d^{xy}_{i,j+1}\phi^{xy}_{i,j+1} + d^{xy}_{i,j-1}\phi^{xy}_{i,j-1} \\
&\qquad + (c^{xy}_{i-1,j}\phi^y_{i,j} + \tilde{c}^{xy}_{i-1,j}\phi^{xy}_{i,j}) + (\tilde{c}^{xy}_{i+1,j}\phi^{xy}_{i,j} - c^{xy}_{i+1,j}\phi^y_{i+1,j}) \\
&\qquad + (c^{xy}_{i,j-1}\phi^x_{i,j} + \tilde{c}^{xy}_{i,j-1}\phi^{xy}_{i,j}) + (\tilde{c}^{xy}_{i,j+1}\phi^{xy}_{i,j} - c^{xy}_{i,j+1}\phi^x_{i,j+1}) + S^{xy}_{ui,j}
\end{aligned} \tag{27}$$

The convective fluxes pertaining to each of the four NIMO grids are shown in Figure 4. The proper locations of the fluxes entering or leaving CV, CV^x, CV^y and CV^{xy} are shown clearly in Figure 4.

DOI: 10.1002/fld

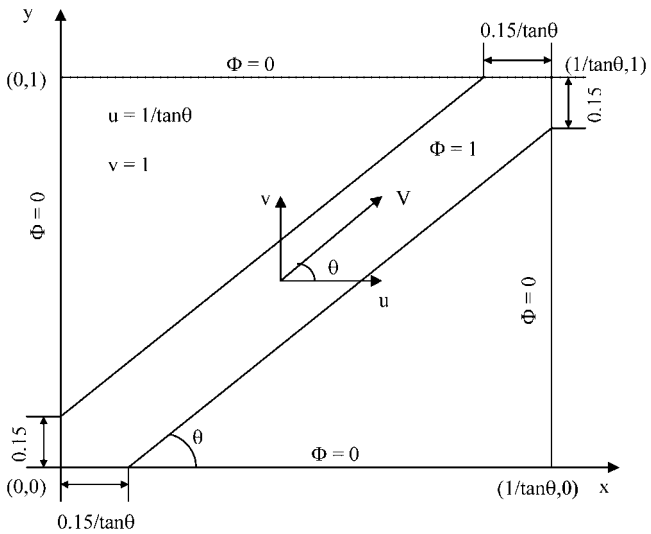

Figure 5. Computational domain of the test problem of inclined flow at angle θ with double step change in passive scalar variable ϕ from 0 to 1.

Interpretation of the above general NIMO equations is not easy. This interpretation will be left after reducing the above equation to the test problem, which will be shown in Figure 5.

THE FIRST TEST PROBLEM

The first test problem chosen to check the present NIMO scheme is shown in Figure 5. This oblique flow configuration was also used by Song *et al.* [8–10] to test their fourth-order schemes. A similar test problem with a single step change in ϕ was utilized by Raithby [11] and Verma and Eswaran [12]. The limiting case of the flow configuration of Figure 5 with infinite Peclet number has an exact analytical solution. In this case, with the absence of diffusion, the value of ϕ remains constant in the vicinity of the diagonal of the solution domain at a value of 1.0 while ϕ assumes a value of zero elsewhere, as shown in Figure 5. The variable ϕ is a passive scalar that has a vanishing source term. The test problem solution domain is $(1/\tan\theta \times 1)$ while the velocity components (u and v) are equal to $1/\tan\theta$ and 1.0, respectively. The density is also taken as constant and equal to 1.0. The width along the x-coordinate, for $y=0.0$ and $\phi=1.0$, is equal to $(0.15/\tan\theta)$ while along the y-coordinate, at $x=0.0$, it is 0.15, as shown in Figure 5. All the above values are in SI units. The boundary condition is also shown in Figure 5, with $\phi=1.0$ in a districted zone and zero everywhere on the solution domain boundaries. The cell Peclet number at any node (i, j) is defined as

$$Pe_{i,j} = |c_{i,j}|/d_{i,j} \tag{28}$$

For uniform convection and diffusion fluxes, the cell Peclet number is also uniform; otherwise it will be grid-node dependent.

DOI: 10.1002/fld

For the test problem of Figure 5, the values of source terms and the fluxes coefficients in Equations (20), (25)–(27) are

$$S_{pi,j}=0; \quad S_{ui,j}=0 \tag{29}$$

$$\hat{c}_{i-1,j}=c_{i-1,j}; \quad \hat{c}_{i,j-1}=c_{i,j-1} \tag{30}$$

$$\tilde{c}_{i-1,j}=0; \quad \tilde{c}_{i,j-1}=0 \tag{31}$$

$$\hat{c}_{i+1,j}=0; \quad \hat{c}_{i,j+1}=0 \tag{32}$$

$$\tilde{c}_{i+1,j}=c_{i+1,j}; \quad \tilde{c}_{i,j+1}=c_{i,j+1} \tag{33}$$

Similarly, the values of $\hat{c}$ and $\tilde{c}$ in the other three control volumes, CV^x, CV^y and CV^{xy}, can be obtained. The NIMO finite-difference equations for the test problem can thus be obtained from Equations (20), (25)–(27) as follows:

$$\begin{aligned}
&[d_{i+1,j}+(d_{i-1,j}+c_{i-1,j})+d_{i,j+1}+(d_{i,j-1}+c_{i,j-1})]\phi_{i,j}\\
&\quad=d_{i+1,j}\phi_{i+1,j}+d_{i-1,j}\phi_{i-1,j}+d_{i,j+1}\phi_{i,j+1}+d_{i,j-1}\phi_{i,j-1}\\
&\qquad+c_{i-1,j}\phi^x_{i-1,j}+c_{i+1,j}(\phi_{i,j}-\phi^x_{i,j})\\
&\qquad+c_{i,j-1}\phi^y_{i,j-1}+c_{i,j+1}(\phi_{i,j}-\phi^y_{i,j})
\end{aligned} \tag{34}$$

$$\begin{aligned}
&[d^x_{i+1,j}+(d^x_{i-1,j}+c^x_{i-1,j})+d^x_{i,j+1}+(d^x_{i,j-1}+c^x_{i,j-1})]\phi^x_{i,j}\\
&\quad=d^x_{i+1,j}\phi^x_{i+1,j}+d^x_{i-1,j}\phi^x_{i-1,j}+d^x_{i,j+1}\phi^x_{i,j+1}+d^x_{i,j-1}\phi^x_{i,j-1}\\
&\qquad+c^x_{i-1,j}\phi_{i,j}+c^x_{i+1,j}(\phi^x_{i,j}-\phi_{i+1,j})\\
&\qquad+c^x_{i,j-1}\phi^{xy}_{i,j-1}+c^x_{i,j+1}(\phi^x_{i,j}-\phi^{xy}_{i,j})
\end{aligned} \tag{35}$$

$$\begin{aligned}
&[d^y_{i+1,j}+(d^y_{i-1,j}+c^y_{i-1,j})+d^y_{i,j+1}+(d^y_{i,j-1}+c^y_{i,j-1})]\phi^y_{i,j}\\
&\quad=d^y_{i+1,j}\phi^y_{i+1,j}+d^y_{i-1,j}\phi^y_{i-1,j}+d^y_{i,j+1}\phi^y_{i,j+1}+d^y_{i,j-1}\phi^y_{i,j-1}\\
&\qquad+c^y_{i-1,j}\phi^{xy}_{i-1,j}+c^y_{i+1,j}(\phi^y_{i,j}-\phi^{xy}_{i,j})\\
&\qquad+c^y_{i,j-1}\phi_{i,j}+c^y_{i,j+1}(\phi^y_{i,j}-\phi_{i,j+1})
\end{aligned} \tag{36}$$

$$\begin{aligned}
&[d^{xy}_{i+1,j}+(d^{xy}_{i-1,j}+c^{xy}_{i-1,j})+d^{xy}_{i,j+1}+(d^{xy}_{i,j-1}+c^{xy}_{i,j-1})]\phi^{xy}_{i,j}\\
&\quad=d^{xy}_{i+1,j}\phi^{xy}_{i+1,j}+d^{xy}_{i-1,j}\phi^{xy}_{i-1,j}+d^{xy}_{i,j+1}\phi^{xy}_{i,j+1}+d^{xy}_{i,j-1}\phi^{xy}_{i,j-1}\\
&\qquad+c^{xy}_{i-1,j}\phi^y_{i,j}+c^{xy}_{i+1,j}(\phi^{xy}_{i,j}-\phi^y_{i+1,j})\\
&\qquad+c^{xy}_{i,j-1}\phi^x_{i,j}+c^{xy}_{i,j+1}(\phi^{xy}_{i,j}-\phi^x_{i,j+1})
\end{aligned} \tag{37}$$

DOI: 10.1002/fld

It should be mentioned here that all the above convective fluxes are positive in the case of the first test problem shown in Figure 5. This is because all the velocity components in the solution domain are positive, as shown in Figure 5.

The above equations share one feature with the pure upwind method. This shared feature is, namely, the left-hand side of the above equations. However, the right-hand sides of the NIMO equations are essentially different, as it accommodates the outgoing fluxes that are ignored in the upwind scheme. Each NIMO control volume receives incoming convective fluxes from two other grids, e.g. the main CV receives two incoming convective fluxes from the x- and y-grids. In addition to the incoming upwind flux effects, the outgoing fluxes have a unique perturbation. The outgoing fluxes leave traces behind in the control volumes, as can be seen from the last terms of Equations (34)–(37) or their general forms above. These traces are the outcome of the differences between the CV center ϕ and the leaving ϕ values. Positive and negative traces are possible. While the incoming fluxes of ϕ tend to increase the CV central values, the traces may increase or decrease ϕ at the center of the control volume of the grid in question. Each grid receives fluxes from neighboring grids as well as traces resulting from the leaving fluxes of ϕ to the same neighboring grids, as can be seen from the above set of equations defining the NIMO scheme. The net gain in each control volume is redistributed by the diffusion mechanism, as dictated by the NIMO finite-difference equations above. The interpretations of the reduced NIMO finite-difference equations, reflecting the test problem flow conditions, apply equally to their general counterparts.

NUMERICAL RESULTS OF THE FIRST TEST PROBLEM

The solution to the test problem is obtained numerically. The TDMA, line-by-line ADA, is adopted [1]. Equations (34)–(37) are modified at the nodes adjoining the boundary to satisfy the conditions imposed there. The value of the cell Peclet number is fixed at a very large number to simulate $Pe=\infty$ of the limiting case of the test problem. A value of $Pe>10^4$ is found sufficient enough to essentially suppress diffusion transport from Equations (34)–(37). The NIMO simulation results shown in Figure 6 are obtained for a fixed value of $Pe=10^6$. The NIMO solution procedure computes the diffusive fluxes from the given Peclet number and Equation (28). Different grids are used for the 45° oblique flow for the four grids of the NIMO scheme. These grids are one square grid (59×59), two rectangular grids (59×69 and 59×53) and one non-uniform grid (59×69). However, a uniform 99×59 grid is utilized for the 30° oblique flow. These different meshes are used to explore the behavior of the NIMO scheme under conditions imposed by square, rectangular and non-uniform grids. Under-relaxation factors (URF) in the range of 0.3–0.5 for the 45° oblique flow and 0.6 for the 30° oblique flow are used for the finite-difference equations of each grid. The above ranges are convenient to control the conversion processes of the interlinked variables ϕ, ϕ^x, ϕ^y and ϕ^{xy} of the NIMO scheme. The number of iterations and the residual errors of each grid are discussed below. Figure 6 depicts the results of Song *et al.* [8–10] for different single-grid schemes and the present results of the hybrid single-grid and NIMO schemes, for $\theta=45°$. The exact solution is also shown in Figure 6. The present results of the multi-grid system (NIMO) gave a numerical solution that exactly fits the analytical solution of the limiting case, when $Pe=\infty$. No overshooting, undershooting or false diffusion can be detected from the present results. It can be noted that the NIMO scheme essentially predicts the proper infinite gradient of ϕ at $y=0.35$ and 0.65, as shown in Figure 6. Moreover, the hybrid scheme, with its dominant false diffusion,

DOI: 10.1002/fld

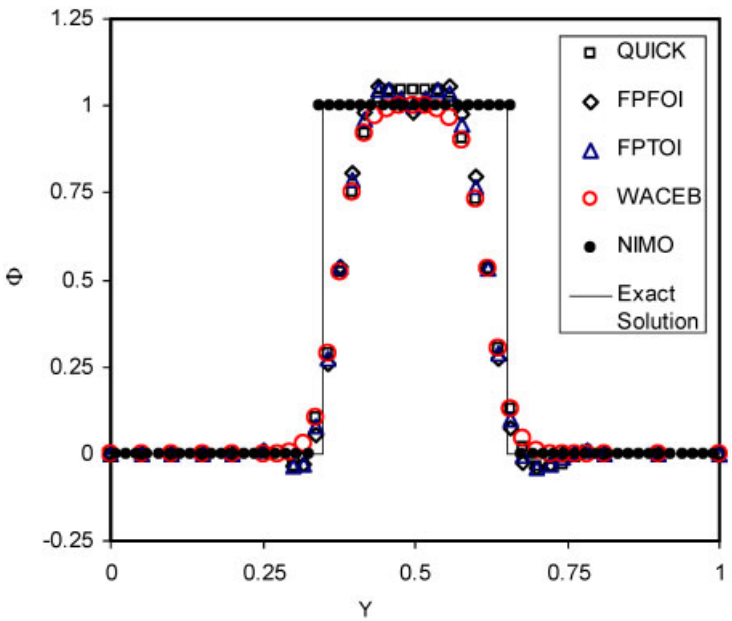

Figure 6. Profiles of ϕ for previous numerical schemes and NIMO at $x=0.5$ and $Pe=\infty$ for 59×59 square grid and $\theta=45°$.

gave the least agreement with the analytical solution. The FPFOI, FPTOI and WACEB schemes are much better than the hybrid scheme. However, FPFOI and FPTOI schemes [8] suffer from overshooting and undershooting and were unable to predict the infinite $(\mathrm{d}\phi/\mathrm{d}y)$ at $y=0.35$ and 0.65. Although the WACEB scheme [9, 10] results are properly bounded between zero and one, it still could not predict the infinite gradient of ϕ at $y=0.35$ and 0.65, as can be seen from Figure 6.

It seemed interesting to see how NIMO works for values of Peclet number less than infinity. Numerical results of ϕ are also obtained for the same boundary conditions and using the 45° oblique flow. The NIMO scheme profiles of ϕ along the y-axis and at $x=0.5$ for $Pe=10, 50, 200$ and 1000 are shown in Figure 7. The hybrid results for $Pe>2$ and the analytical solution, for $Pe=\infty$, were re-plotted in Figure 7 for comparison. It can be seen that as Pe increases, $(\mathrm{d}\phi/\mathrm{d}y)$, at $y=0.35$ and 0.65, increases. When $Pe=1000$, $(\mathrm{d}\phi/\mathrm{d}y)$ is so steep that it almost reaches infinity.

The four-grid values of the passive scalar variable, i.e. ϕ, ϕ^x, ϕ^y and ϕ^{xy}, are plotted in Figure 8. The profiles of the scalar variable are plotted at $x=0.5$ for a value of Peclet number equals to 5. The values of ϕ^x and ϕ^{xy} at $x=0.5$ used in Figure 8 have been obtained by interpolating the converged final solution due to the shifting of the x- and xy-grids with respect to $x=0.5$ plane. The four profiles fall on top of each other indicating that the fields of ϕ, ϕ^x, ϕ^y and ϕ^{xy} converge together to essentially the same values. The accuracy of each grid of NIMO is accessed by computing the sum, over all nodes, of the absolute residual errors. The residual error at a node of each grid is computed as the imbalance of the pertinent finite-difference equation.

DOI: 10.1002/fld

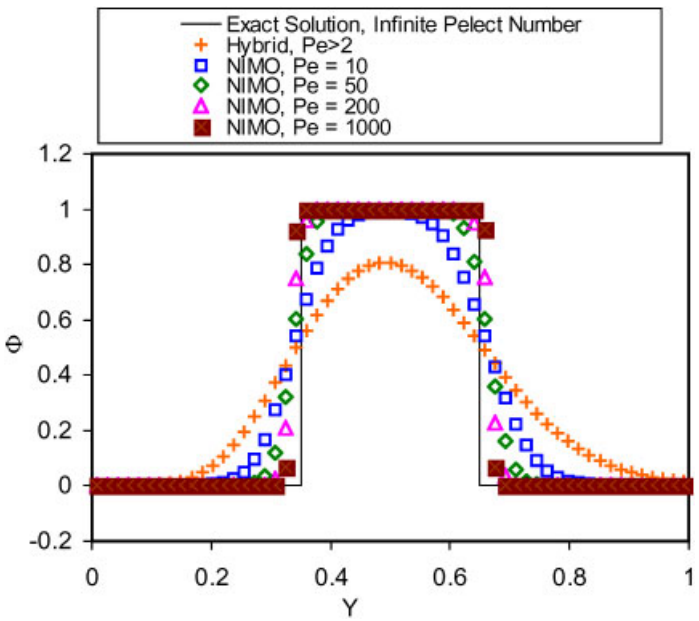

Figure 7. Profiles of ϕ at $x=0.5$ for $Pe=10$, 50, 200 and 1000 and exact solution for $Pe=\infty$ for 59×59 square grids and $\theta=45°$.

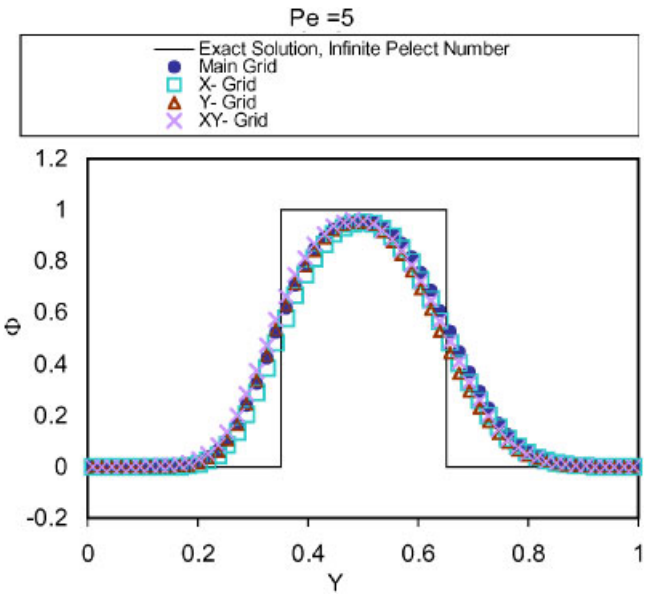

Figure 8. Profiles of ϕ, ϕ^x, ϕ^y and ϕ^{xy} at $x=0.5$ for $Pe=5$ for 59×59 square grids and $\theta=45°$.

DOI: 10.1002/fld

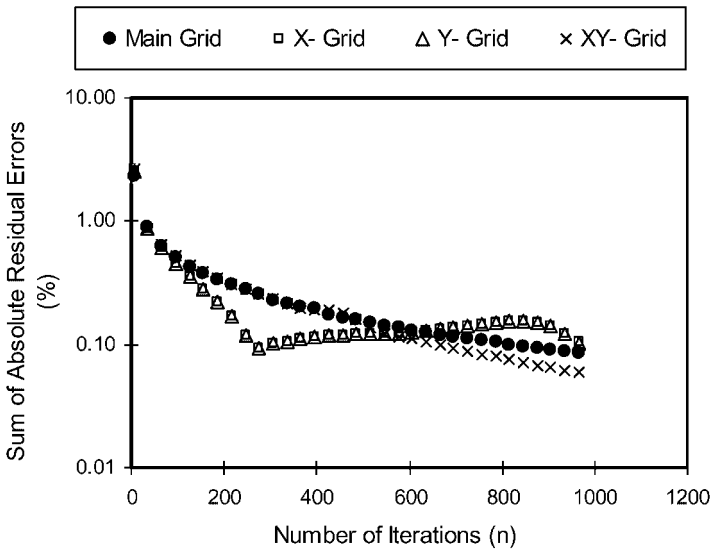

Figure 9. Percentage sum of absolute residual errors of the finite-difference equations of the main, x-, y- and xy-grids of NIMO for $Pe=5$ for 59×59 square grids and $\theta=45°$.

The sums of absolute residual errors of the main, x-, y- and xy-grids are plotted as a percentage of the incoming total fluxes of ϕ *versus* the number of iterations (n) in Figure 9, for $Pe=5$ and URF$=0.3$. The iterations are stopped when the maximum error of any grid is less than 0.1%. This condition is satisfied when $n=975$. The above conversion criterion is also nearly satisfied near $n=600$. However, the larger number of iterations is favored to insure complete conversion. The pattern of changes of the error curves is very interesting. The main grid and xy-grid errors are similar and decrease monotonically. However, the x-grid and y-grid errors are nearly identical, as can be seen from Figure 9. They converge faster at the beginning and then suddenly diverge slightly only to converge to the desired accuracy at 975 iterations. Part of the faster convergence at the beginning is attributed to the fact that four sweeps per iteration were used for the x- and y-grids, while only two sweeps per iteration proved to be sufficient for the main and the xy-grids. It is interesting to note that the four grids interact in such a way that the main and the xy-grids have no direct link. However, they are linked indirectly through their interactions with both x- and y-grids. On the other hand, the x- and y-grids establish their indirect link by interacting directly with both main and xy-grids. The interlinking of the grids explains the pairing of the sum of the absolute residual errors of the main and xy-grids as well as the pairing the x- and y-grids. It should be mentioned that the initial error, which is approximately equal to 3.4, arises from the initial guess. The exact analytical solution to the test problem is used as the initial guess for ϕ, ϕ^x, ϕ^y and ϕ^{xy} for all runs reported in the present work.

NIMO and hybrid profiles of ϕ are shown in Figure 10, for $Pe=1.0$ and $x=0.5$. In this case, ϕ is equally transported by convection and diffusion. Figure 10 shows that the hybrid scheme produced skewed profiles of ϕ along the y-axis, while NIMO properly predicts symmetrical profiles. The skewed part of ϕ is an outcome of the inevitable false diffusion of the hybrid scheme, which results from blowing wind along the positive direction of the y-axis. This can also be detected from the

DOI: 10.1002/fld

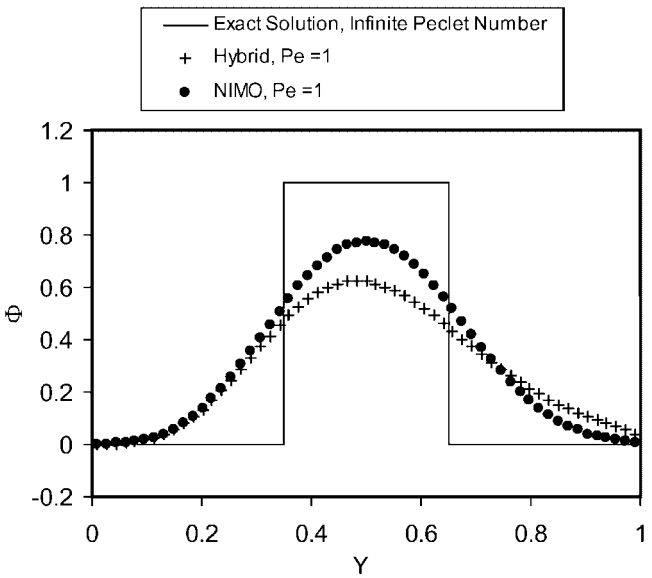

Figure 10. Profiles of ϕ for NIMO and hybrid schemes at $x=0.5$ for $Pe=1$ for 59×59 grids and $\theta=45°$.

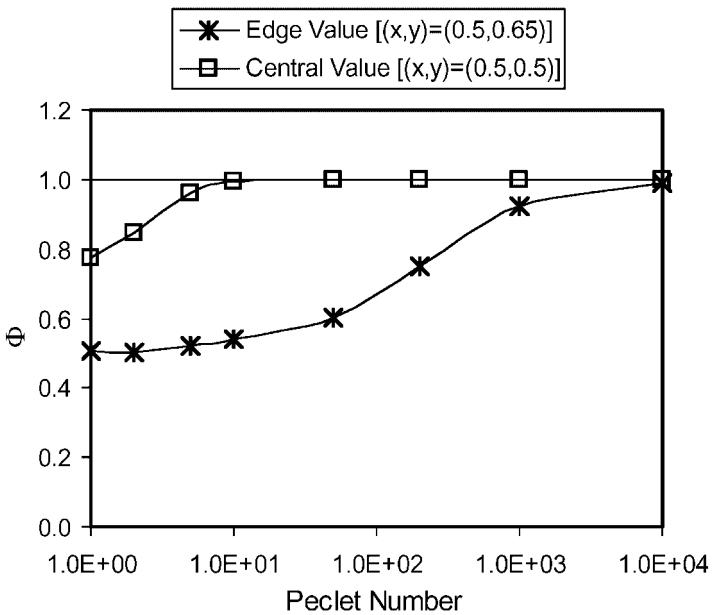

Figure 11. NIMO values of ϕ at the edge $[(x, y)=(0.5, 0.65)]$ and center of the solution domain $[(x, y)=(0.5, 0.5)]$ *versus* Peclet number for 59×59 square grids and $\theta=45°$.

DOI: 10.1002/fld

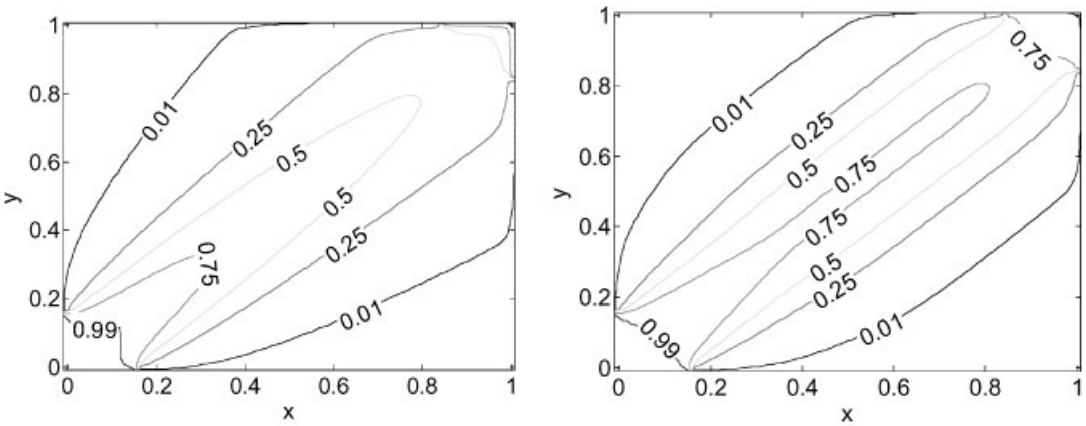

Figure 12. Contour plots of ϕ for unity Peclet number for 59×59 square grids and $\theta = 45°$: (a) hybrid, $Pe = 1$ and (b) NIMO, $Pe = 1$.

hybrid scheme profile of ϕ, for $Pe > 2.0$, which is shown in Figure 7. Similar skewed profiles of ϕ were also obtained by Song *et al.* [9–11], for $Pe > 2.0$. It can be seen from Figure 10 that the central value of ϕ is higher in the case of NIMO. This is because the hybrid scheme suffers from extra numerical diffusion, as shown in Figure 10.

It is also interesting to determine the minimum Peclet number that produces essentially a flat profile of ϕ along the y-axis for $0.35 < y < 0.65$. This is achieved in Figure 11 by plotting the value of ϕ along the edge and center of the diagonal edge *versus Pe*. A value of 10^4 is just sufficient for *Pe* to produce nearly diffusion-free results.

The ϕ contours that produced Figure 11 are shown in Figure 12. The skewed ϕ profile of the hybrid scheme along the y-coordinate direction is also obvious from Figure 12(a). However, the hybrid scheme contours appear to be nearly symmetrical around the diagonal of the solution domain, as this is the true flow direction. Moreover, the NIMO results indicate that ϕ is more contained inside the zone bounded by $y = 0.35$ and 0.65, as can be seen from Figure 12(b).

More contours are plotted in Figure 13. The additional NIMO contours are for $Pe = 10$, 50, 200 and 1000. Figure 13(a) shows hybrid scheme ϕ contours for $Pe > 2.0$. The hybrid contours show that ϕ remains close to unity in a very small area next to the inlet section where ϕ assumes a value of 1.0. However, the NIMO contours show that the area where ϕ remains uncontaminated increases as the Peclet number increases. Finally at $Pe = 10^3$, most of the core along the diagonal of the solution domain is filled with unity ϕ fluid, as can be seen from Figure 13(e). Moreover, the widths of the narrow strips, bounded by $\phi = 0.99$ and 0.01, that surround the diagonal core decrease as Peclet number increases. These narrow strips become nearly nonexistent as the Peclet number increases beyond 10^3. In order to find out how much NIMO is dependent on the boundary conditions, along the exit sections of the solution domain, a few computer runs were performed. These runs had zero ϕ gradients at the exit section instead of the fixed-ϕ-value boundary condition. These runs, although not reported here, showed that the NIMO scheme is not sensitive to this change in boundary condition for the flow configuration of Figure 5 except for the nodes very near to the exit boundary of the solution domain. For these nodes, insignificant differences of the order of $\pm 0.1\%$, between zero-gradient and fixed-value boundary conditions, were encountered.

DOI: 10.1002/fld

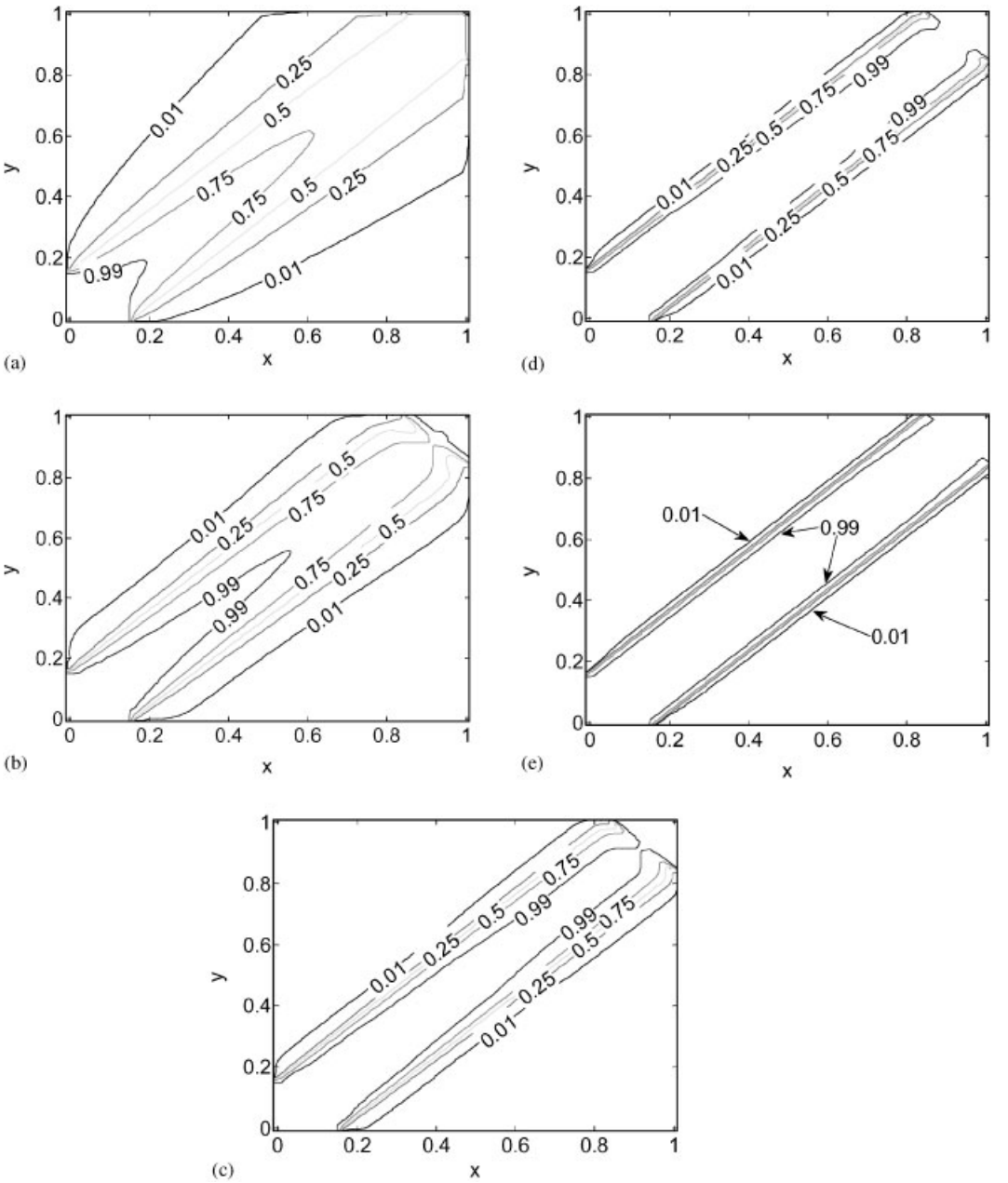

Figure 13. Contour plots of ϕ for hybrid scheme ($Pe>2$) and NIMO system (59×59 square grids, $\theta=45^\circ$ and $Pe=10$, 50, 200 and 10^3): (a) hybrid, $Pe>2$; (b) NIMO, $Pe=10$; (c) NIMO, $Pe=50$; (d) NIMO, $Pe=200$; and (e) NIMO, $Pe=10^3$.

DOI: 10.1002/fld

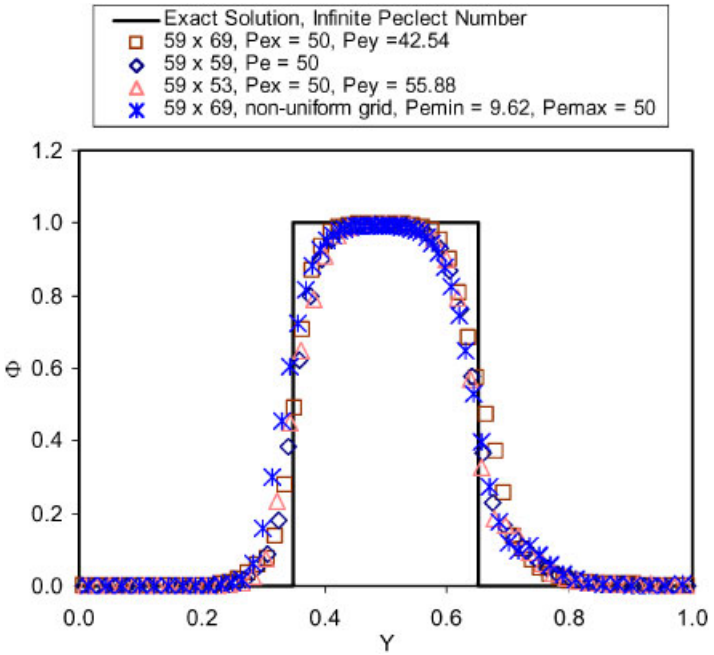

Figure 14. Profiles of ϕ at $x=0.5$, for different grid dimensions and geometries, for Peclet numbers along the x-axis equal to 50 and $\theta=45°$.

In order to check the consistency of the NIMO scheme, a number of meshes were used to compute the oblique flow of Figure 5, for $\theta=45°$. All the grids have 59 nodes along the x-coordinate, while 53, 59 and 69 nodes are used along the y-coordinate. One of these grids is non-uniform (59×69), whereas the other three are uniform (59×53, 59×59 and 59×69). The scalar variable profiles, along the $x=0.5$ plane, are shown in Figures 14 and 15, for two nominal values of the Peclet number, namely 50.0 and 1000.0. Only the (59×59) square grid has uniform Peclet number. However, the rectangular uniform grids have Peclet number values along the y-axis higher or lower than the nominal value along the x-axis. This is because Δx does not equal Δy for the rectangular grids, while the fluid physical properties are uniform and $u=v$ for the 45° flow. Moreover, the non-uniform grid has Peclet numbers that are space dependent. For a nominal Peclet number of 50.0, the profiles of ϕ at $x=0.5$ for the above-mentioned grid dimensions are in good agreement with each other, as shown in Figure 14. The minor differences between them arise from the non-uniformity of the Peclet number of the rectangular and non-uniform grids, as can be seen from Figure 14.

The profiles of ϕ for different grid geometries and dimensions are shown in Figure 15, for a nominal Peclet number of 1000.0 and $\theta=45°$. The (59×69) non-uniform grid is uniform along the x-coordinate and non-uniform along the y direction. The (59×69) grid contracts along the y-coordinate from the outer boundaries towards the center where $y=0.5$. For this grid, the ratio of the maximum increment to the minimum increment along the y-coordinate is 4.5. The profiles essentially capture the analytical solution for infinite Peclet number and $\theta=45°$, although they were computed for different grid geometries and dimensions. It can be concluded that irrespective of the

DOI: 10.1002/fld

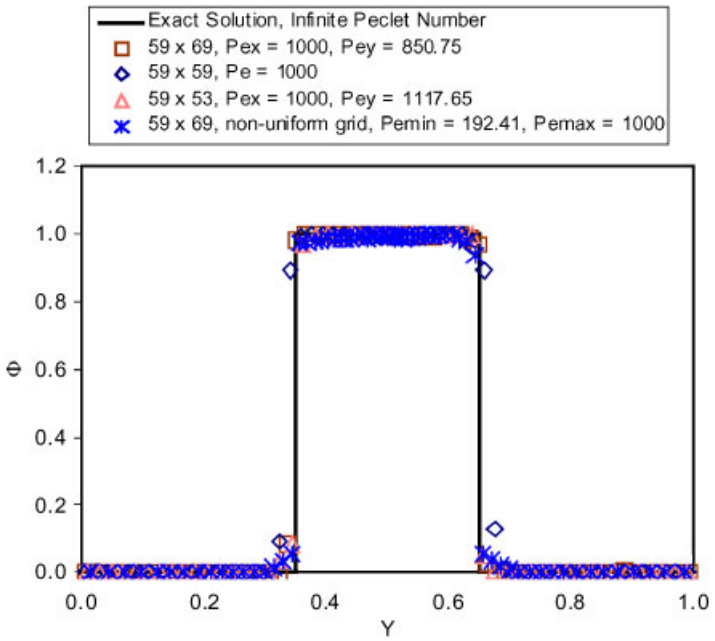

Figure 15. Profiles of ϕ at $x=0.5$, for uniform and non-uniform different grid dimensions, for Peclet numbers along the x-axis equal to 1000 and $\theta=45°$.

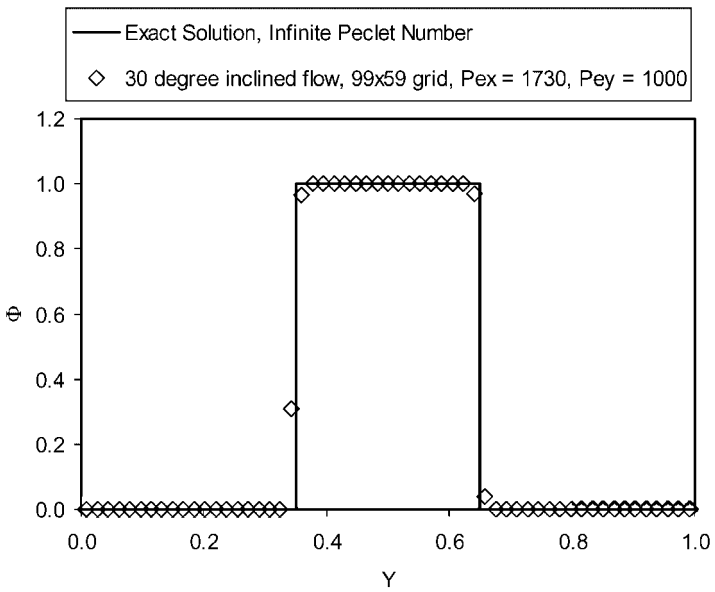

Figure 16. Profiles of ϕ at $x=0.5/\tan\theta$, for 99×59 grids, for Peclet numbers along the y-axis equal to 1000 and $\theta=30°$.

DOI: 10.1002/fld

dimensions or geometry of the computational grid, the NIMO scheme is capable of computing the exact solution. However, the skewed upstream-differencing scheme of Raithby [11] can capture the exact solution only for square grids where the diagonals of the computational cells are parallel and normal to the flow direction.

Another test is introduced in Figure 16 for an angle of inclination of 30°. In this case, the oblique flow passes diagonally through a rectangular solution domain. The distance of the solution domain and the velocity component along the x-axis are approximately equal to 1.73. The grid used for the profiles in Figure 16 has dimensions of 99×59. The Peclet numbers along the x- and y-axes are 1730 and 1000, respectively. Here also, none of the computational cell diagonals is parallel or normal to the flow direction. However, the profile of ϕ captures the exact analytical solution for infinite Peclet numbers, as can be seen from Figure 16.

THE SECOND TEST PROBLEM

The second test problem is chosen in the cylindrical-polar domain. It is chosen to check the accuracy and applicability of the NIMO numerical scheme in coordinates with curvature. The configuration is that of a rotating radial flow in an annular sector. The velocity field is prescribed as shown in Figure 17. The tangential velocity u is taken as uniform and is equal to unity, while the radial velocity v is inversely proportional to the radial distance r. This velocity configuration satisfies the mass continuity of the constant-density rotating radial flow in an annular sector.

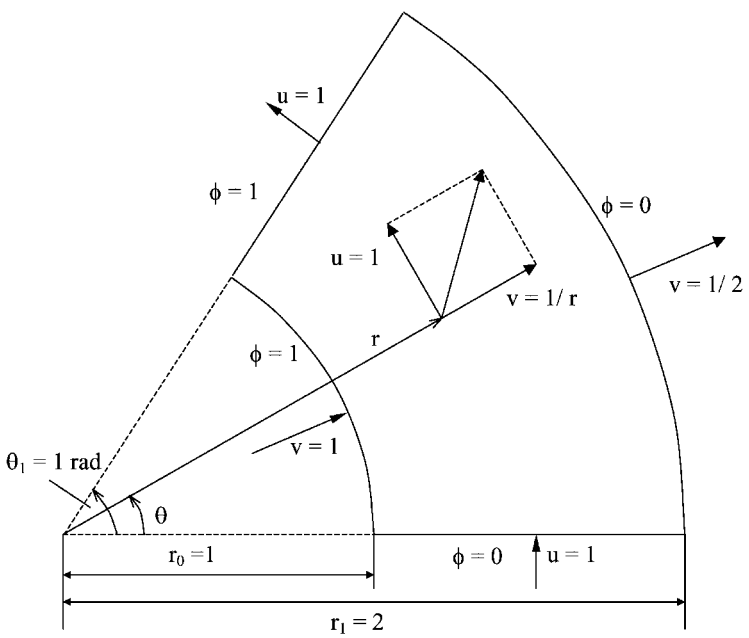

Figure 17. Cylindrical-polar computational domain of the test problem of rotating radial flow in an annular sector with a single step change in passive scalar variable ϕ from 0 to 1.

DOI: 10.1002/fld

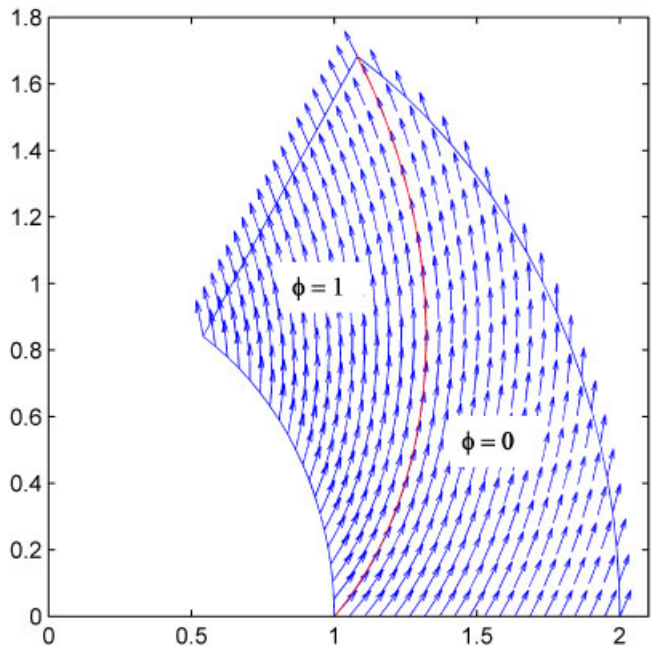

Figure 18. Velocity vector field for rotating radial flow in an annular sector, showing the boundary curve between regions of $\phi = 1$ and 0 in r–θ plane, for infinite Peclet number.

The annular sector is bounded by $r_0 = 1.0$, $r_1 = 2.0$ and $\theta = 0.0$, $\theta = 1.0$ along the radial and tangential directions, respectively. The passive scalar variable ϕ is equal to 0.0 and 1.0 at the inlet two sections defined by $\theta = 0.0$ and by $r = 1.0$. For infinite Peclet numbers, the exit sections have values of ϕ equals to 1.0 and 0.0 for $\theta = 1.0$ and $r = 2.0$, respectively. For this case the exact solution for the streamline that divides the sector into a $\phi = 0.0$ zone and another zone with $\phi = 1.0$ is shown in Figure 18. The streamline, which runs from point $(1, 0)$ to point $(2, 1)$, is shown in Figure 18, superimposed on the prescribed velocity vector field. The velocity vectors vary in direction and magnitude, which is a good test to the extent of the accuracy of the NIMO numerical scheme in conditions where false diffusion is not uncommon. Equations (20), (25), (26) and (27) are applicable to cylindrical-polar coordinate 2D flows. The superscripts x, y and xy are replaced by θ, r and $r\theta$, while the distances between the central node and the neighboring nodes become $r\delta\theta$ and δr, along the tangential and radial directions, respectively. For this test problem, a 59×59 uniform grid is superimposed on the solution domain of an annular sector. The distances along the tangential (angular) direction, which are involved in the NIMO equations, increase in the radial direction, although the grid itself is uniform.

NUMERICAL RESULTS OF THE SECOND TEST PROBLEM

The numerical solution to the second test problem is also obtained with the TDMA, line-by-line ADA. The value of 10^4 for the cell Peclet number at point $(r, \theta) = (1, 0)$ is found sufficient to

DOI: 10.1002/fld

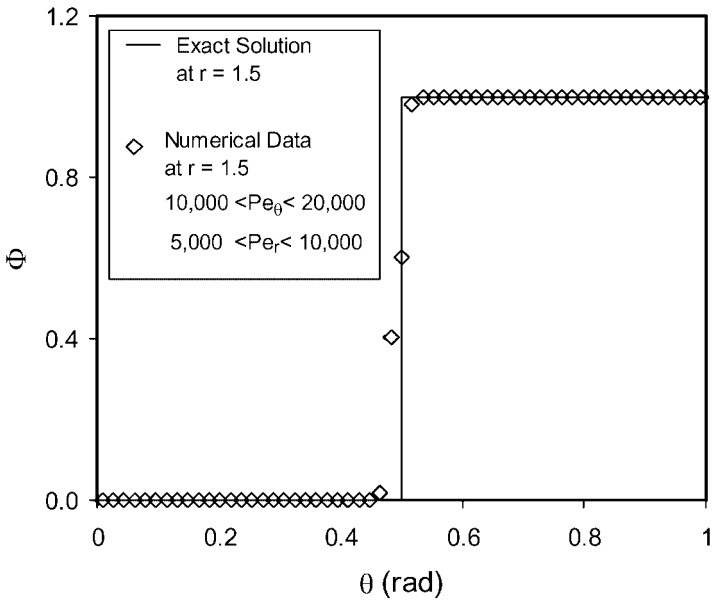

Figure 19. Angular profiles of ϕ, at $r=1.5$, for Peclet numbers ranging from 5000 to 10 000 (angular) and 10 000 to 20 000 (radial), using 59×59 cylindrical-polar grid.

produce nearly diffusion-free profiles of the passive scalar variable. The URF is taken as 0.5, which produced converged solutions after 500 iterations with an error less than 0.1%. The local cell Peclet number along the tangential (angular) direction increases from 10^4 to 2×10^4, while along the radial direction it decreases from 10^4 to 5×10^3. This is an outcome of the variations along the radial direction of the radial velocity and the tangential distance.

Figure 19 shows the angular profiles of the passive scalar variable ϕ computed numerically and the corresponding step function exact solution. The exact solution is obtained for the limiting case of infinite Peclet number. The agreement between the two profiles is excellent. The main differences occur in a very narrow angular zone, where ϕ changes abruptly from 1.0 to 0.0. However, outside this narrow zone, ϕ is properly computed as zero on one side and unity on the other side.

Similarly, the radial profiles of the passive scalar are shown in Figure 20. The NIMO results show an excellent agreement with the exact solution of a step function change in the passive scalar variable. The gradient of the passive scalar along the radial direction $(\delta\phi/\delta r)$ is higher than that along the tangential direction $(\delta\phi/r\delta\theta)$ as can be seen from Figures 19 and 20. This is an outcome of the higher mean value of the Peclet number along the radial direction relative to the corresponding value along the tangential direction.

Figure 21 shows the open contours of ϕ in the rotating radial flow in an annular sector. A thin curved strip, where ϕ varies from 0.001 to 0.999, is computed using the NIMO scheme. Outside this narrow strip the passive scalar variable changes abruptly from 0.0 to 1.0. It is interesting to note the resemblance between the shape of the narrow strip and the exact solution curve that divides the annular sectors into $\phi=0.0$ and 1.0 zones (Figure 18).

DOI: 10.1002/fld

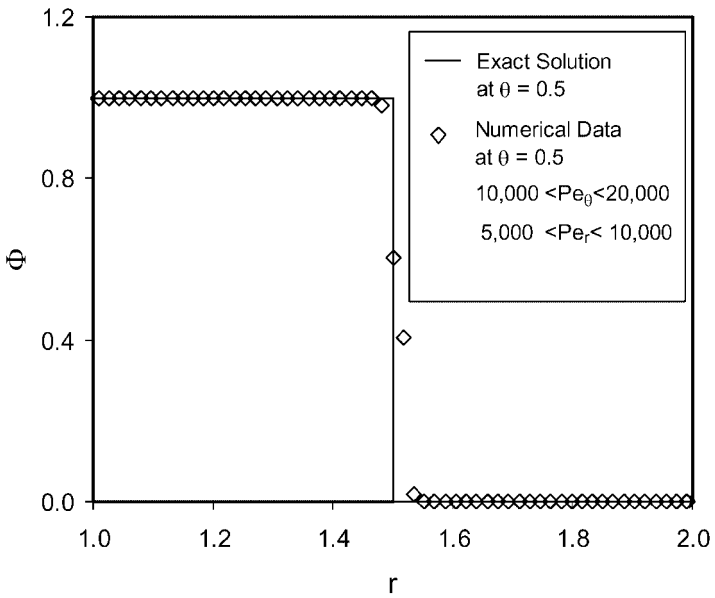

Figure 20. Profiles of ϕ, at $\theta = 0.5$ rad, for Peclet numbers ranging from 5000 to 10 000 (angular) and 10 000 to 20 000 (radial), using 59×59 cylindrical-polar grid.

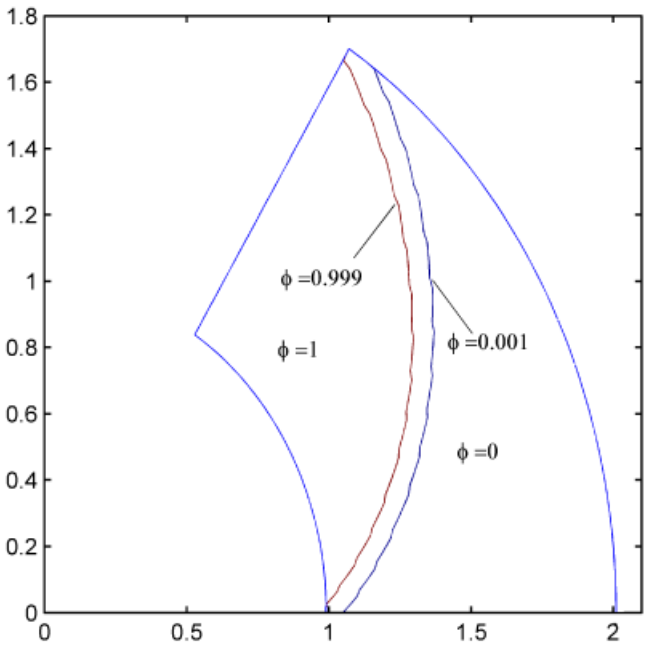

Figure 21. Open contours of the passive scalar variable ϕ for a 59×59 r–θ grid.

DOI: 10.1002/fld

CONCLUSIONS

The present work describes a novel numerical procedure. The new scheme is a non-upwind, interconnected, multi-grid, overlapping (NIMO) finite-difference procedure. The NIMO numerical procedure is free from any interpolations of convective fluxes that normally produce high levels of false diffusion in most known finite-difference schemes. The NIMO system involves four grids in 2D flows. The four grids are located in space such that each grid is displaced midway with respect to one of the remaining grids. The main grid and the *xy*-grid interconnect indirectly through the *x*-grid and the *y*-grid and *vice versa*. Similar interconnection between the four NIMO grids is valid in the cylindrical-polar solution domain. The percentage sum of the absolute residual errors of the main and *xy*-grids behave in the same fashion, which is different from the similar trend of the other two grids. The NIMO scheme is applied to two test problems. The first test problem is the oblique flow in the Cartesian coordinates, while the second test problem is represented by a rotating radial flow in an annular sector. The NIMO finite-difference scheme can produce numerical profiles of ϕ that capture the analytical solution of the test problem for 45 and 30° oblique flows for high Peclet numbers. Moreover, NIMO can essentially capture the analytical solution of the two test problems for square, rectangular and non-uniform grids. The second test problem is also computed with a very high accuracy, which confirms the validity of the NIMO scheme to the cylindrical-polar coordinates as well as to the Cartesian coordinates. Most of the single-grid numerical procedures utilizing rectangular or non-uniform grids could not reach that level of accuracy due to false diffusion, overshooting or undershooting. This could be concluded from the comparison of the data of these schemes with the corresponding present numerical results. The NIMO finite-difference equations contain convective terms that slightly resemble the upwind schemes. However, unlike the upwind scheme, the incoming convective fluxes to a particular grid are supplied by two of the remaining three grids of NIMO. A new feature emerges that allows the outgoing fluxes to leave behind positive or negative traces in a particular grid control volume, which is completely ignored in the upwind scheme. These outgoing convective fluxes constitute the incoming convective fluxes to two of the remaining three grids of NIMO. Results obtained for different values of the Peclet number showed that the diagonal core of the test problem is surrounded by narrow strips bounded by $\phi = 0.99$ and 10^{-2}. These narrow strips become essentially nonexistent as the Peclet number is increased to 10^3. The converged numerical solutions of the four NIMO grids for a passive scalar variable at a fixed value of the Peclet number are consistent and identical.

NOMENCLATURE

A	surface area of control volume
a	finite-difference coefficients
c	convective fluxes
$\hat{c}, \tilde{c}$	modified convective fluxes
d	diffusive fluxes
n	number of iterations
Pe	Peclet number
r	radial direction
S_u, S_p	source term coefficients in linear form
u	velocity component along the x or tangential direction

DOI: 10.1002/fld

u_k	fluid velocity along coordinate direction x_k
v	velocity component along the y or radial direction
x_k	coordinate direction
Γ_ϕ	molecular diffusivity of ϕ
δx	distance between central node and neighboring node
θ	tangential direction or angle of inclination
ρ	density
ϕ	scalar variable

Subscripts

E, W	east and west directions
p	value at the center of control volume
S, N	south and north directions
i, j	grid-node indices

Superscripts

x	x-grid
y	y-grid
xy	xy-grid

REFERENCES

1. Abou-Ellail MMM, Gosman AD, Lockwood FC, Megahed IEA. Description and validation of a three-dimensional procedure for combustion chamber flows. *AIAA Journal of Energy* 1978; **2**:71–80 (also published in *Turbulent Combustion*, Kennedy L (ed.). *AIAA Journal* 1978; **58**:163–190).
2. Patankar SV. *Numerical Heat Transfer and Fluid Flow*. McGraw-Hill: New York, 1980.
3. Roache PJ. *Computational Fluid Dynamics*. Hermosa: Albuquerque, NM, 1972.
4. Prince HS, Varga RS, Warren JE. Application of oscillation matrices to diffusion–convection equations. *Journal of Mathematics and Physics* 1966; **45**:301–311.
5. Leonard BP. A survey of finite differences of opinions on numerical modeling of incomprehensible defective confusion equation. *Winter Annual Meeting*, vol. 34. ASME Applied Mechanics Division: 1979.
6. Leonard BP. Stable and accurate convective modeling procedure based on quadratic upstream interpolation. *Computer Methods in Applied Mechanics and Engineering* 1979; **19**:59–98.
7. Leonard BP. A stable, accurate, economical and comprehendible algorithm for the Navier–Stokes and scalar transport equations. In *Numerical Methods in Laminar and Turbulent Flow*, Taylor C, Schrefler BA (eds), *Proceedings of the Second International Conference*, Venice, Italy, 1981; 543–553.
8. Song B, Liu GR, Lam KY, Amano RS. Four-point interpolation schemes for convective fluxes approximation. *Numerical Heat Transfer*, *Part B* 1999; **35**:23–39.
9. Song B, Liu GR, Lam KY, Amano RS. On a higher-order bounded discretization scheme. *International Journal for Numerical Methods in Fluids* 2000; **32**:881–897.
10. Song B, Liu GR, Amano RS. Applications of a higher-order bound numerical scheme to turbulent flows. *International Journal for Numerical Methods in Fluids* 2001; **35**:371–394.
11. Raithby GD. Skew upstream differencing schemes for problems involving fluid flow. *Computer Methods in Applied Mechanics and Engineering* 1976; **9**:153–164.
12. Verma AK, Eswaran V. Overlapping control volume approach for convection–diffusion problems. *International Journal for Numerical Methods in Fluids* 1996; **23**:865–882.

DOI: 10.1002/fld